Supporting Information

The site pair matching of a tandem Au/CuO–CuO nanocatalyst for promoting the selective electrolysis of CO_2 to C_2 products

*Jun-Hao Zhou[+], Chen-Yue Yuan[+], Ya-Li Zheng, Hai-Jing Yin, Kun Yuan, Xiao-Chen Sun, and Ya-Wen Zhang**

S1. Calculation of Faradaic Efficiency

S1.1 Gaseous Products

$$FE_{gas} = V_i \, x \, flow\ rate \, x \, \frac{nFp0}{RT0i}$$

V_i: the volume concentration of certain product based on a calibration of the GC;
n: number of transferred electrons for certain product;
F: 96485 C mol^{-1};
p_0: 1.013 bar;
R: 8.314 J mol^{-1} K^{-1};
T_0: the temperature for testing;
i: the steady-state current measured during a constant-potential electrolysis.

S1.2 Liquid Products

$$FE_{liquid} = V \, x \, c \, x \, \frac{nF}{Q}$$

V: the volume of the electrolyte in the working cell;
c: the concentration of liquid product after electrolysis, determined by ^1H NMR;
n: number of transferred electrons for certain product;
F: 96485 C mol^{-1}
Q: total charge consumed in the electrolysis.

Supplementary Figures

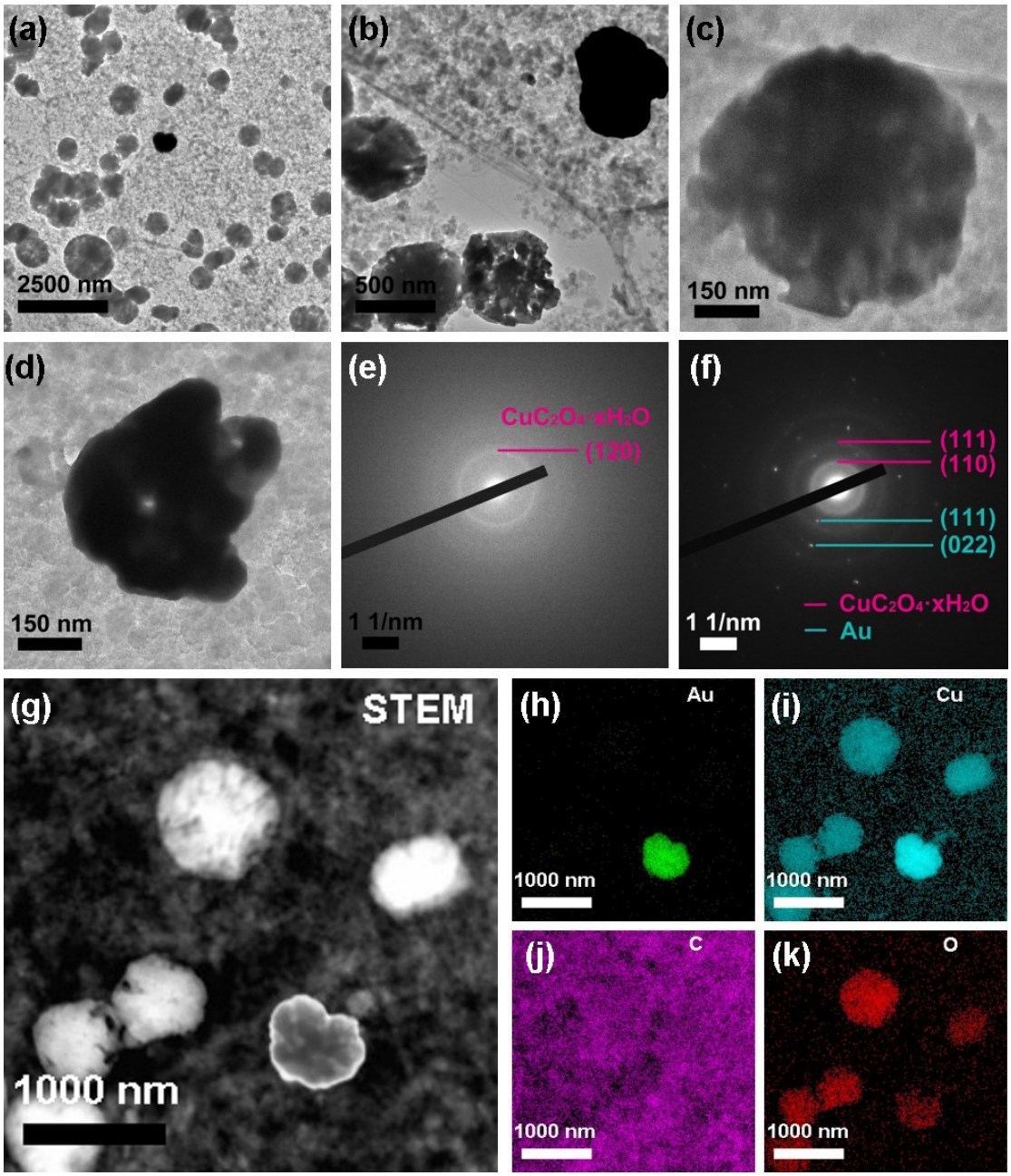

Figure S1. (a) to (d) TEM images of Au/CuC_2O_4/C; (e) and (f) SAED patterns of the particles in c) and d) respectively; (g) to (k) HAADF-STEM image and EDS elemental mappings of Au/CuC_2O_4/C.

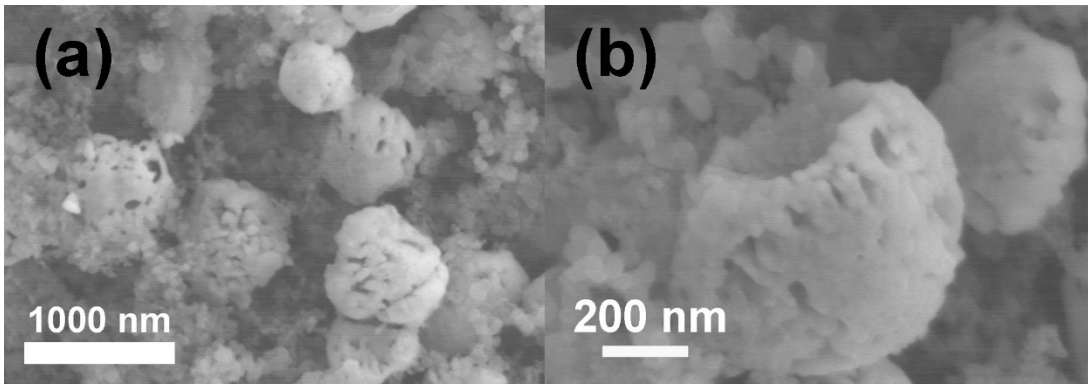

Figure S2. SEM image of Au/CuC_2O_4/C.

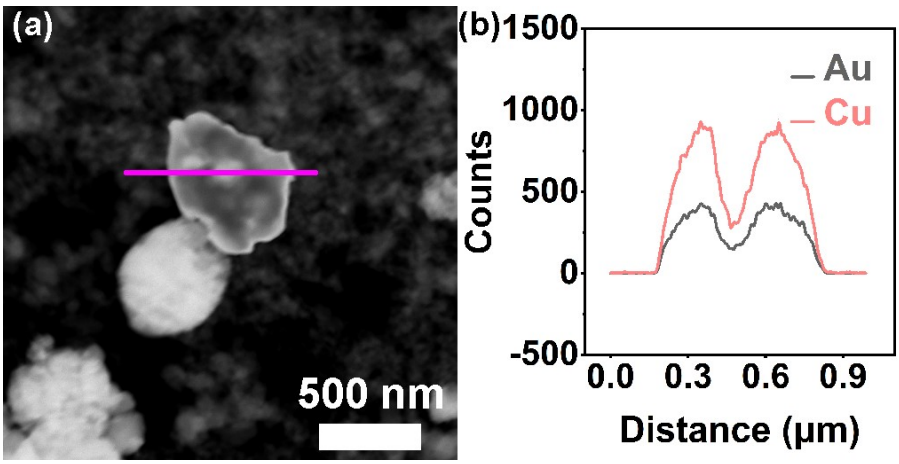

Figure S3. (b) EDS linear scanning result of Au/CuC_2O_4/C, and the scanning area is the violet line in (a).

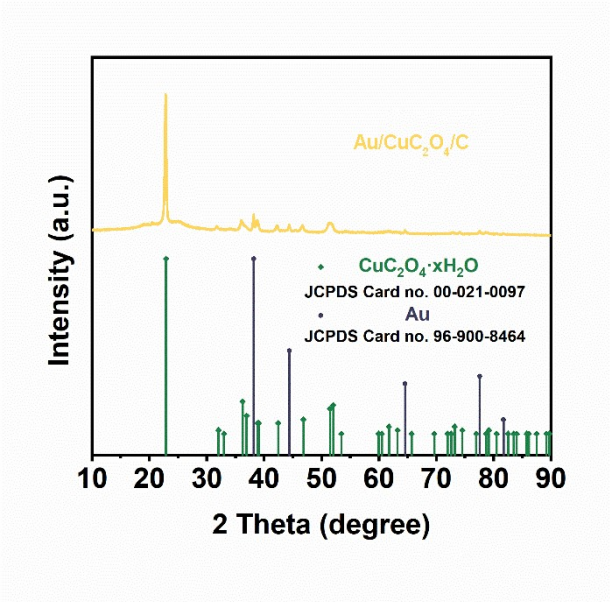

Figure S4. XRD pattern of Au/CuC_2O_4/C.

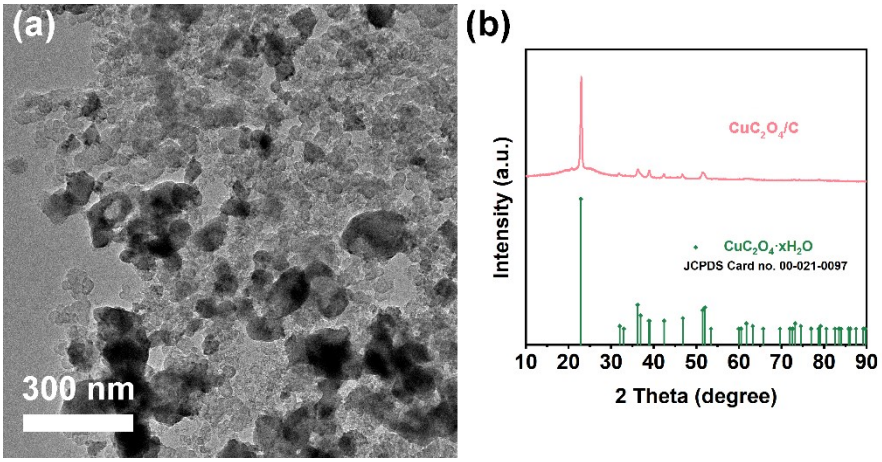

Figure S5. (a) TEM image and (b) XRD pattern of CuC_2O_4/C.

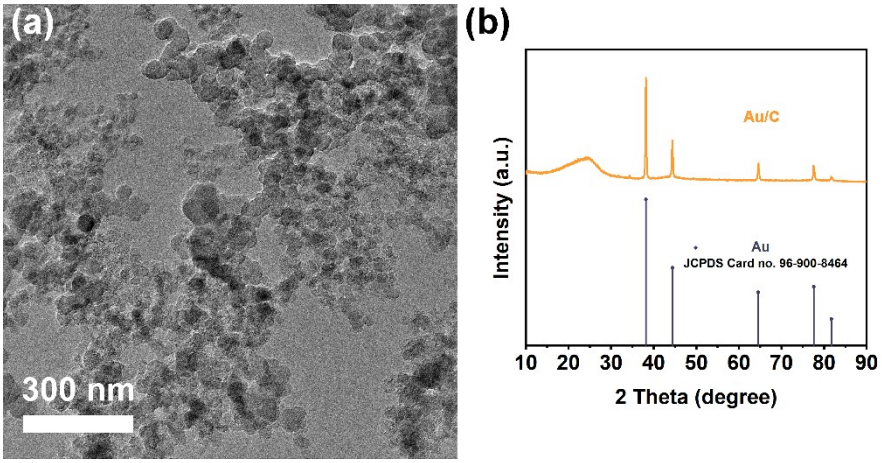

Figure S6. (a) TEM image and (b) XRD pattern of Au/C.

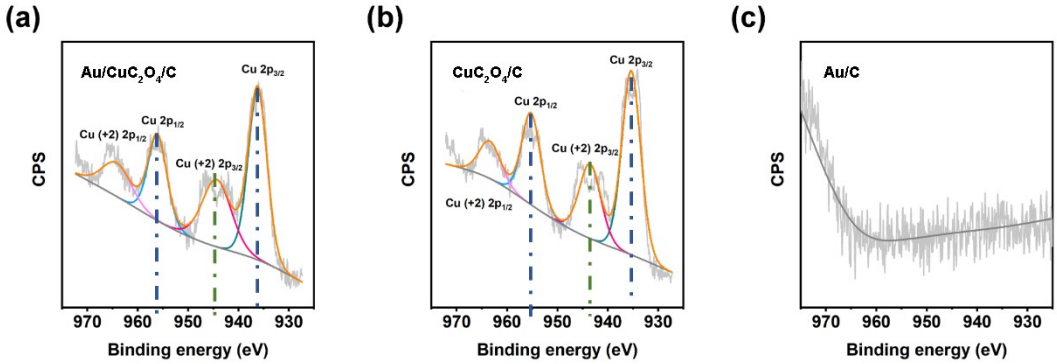

Figure S7. Cu 2p XPS spectra of (a) Au/CuC_2O_4/C, (b) CuC_2O_4/C and (c) Au/C.

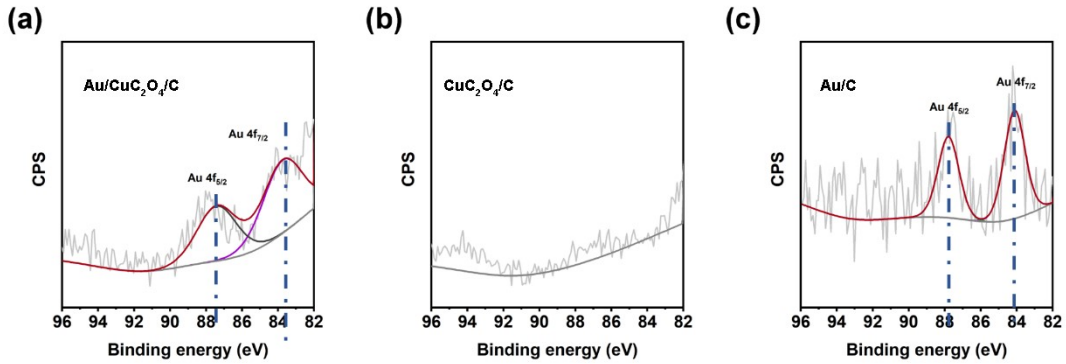

Figure S8. Au 4f XPS spectra of (a) $Au/CuC_2O_4/C$, (b) CuC_2O_4/C and (c) Au/C.

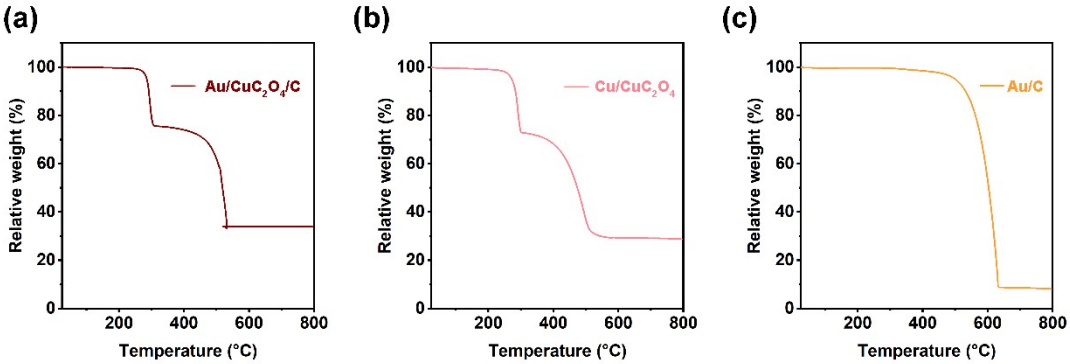

Figure S9. TGA curves of (a) $Au/CuC_2O_4/C$, (b) CuC_2O_4/C and (c) Au/C.

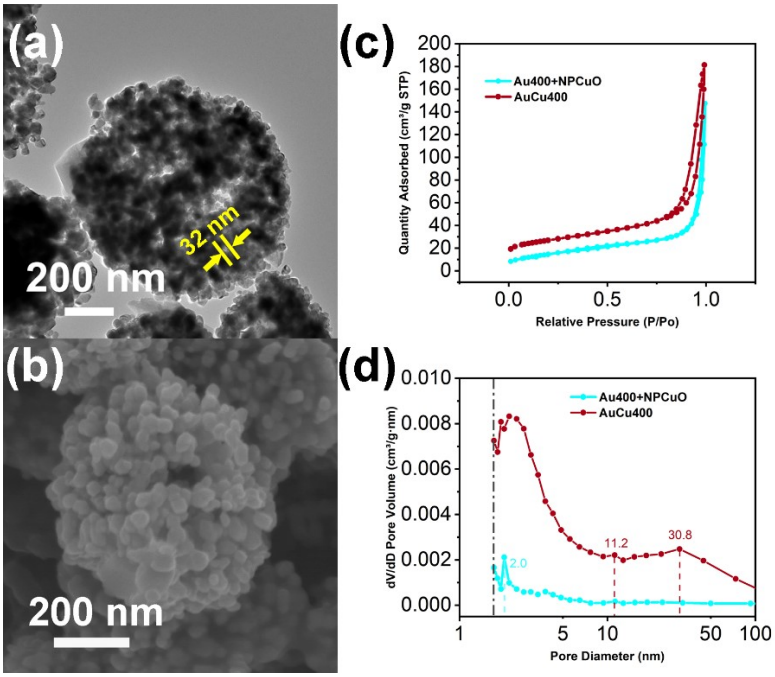

Figure S10. (a) TEM and (b) SEM image of AuCu400; (c) adsorption-desorption isotherms and (d) pore-size distribution curves of AuCu400 and Au400+NPCuO.

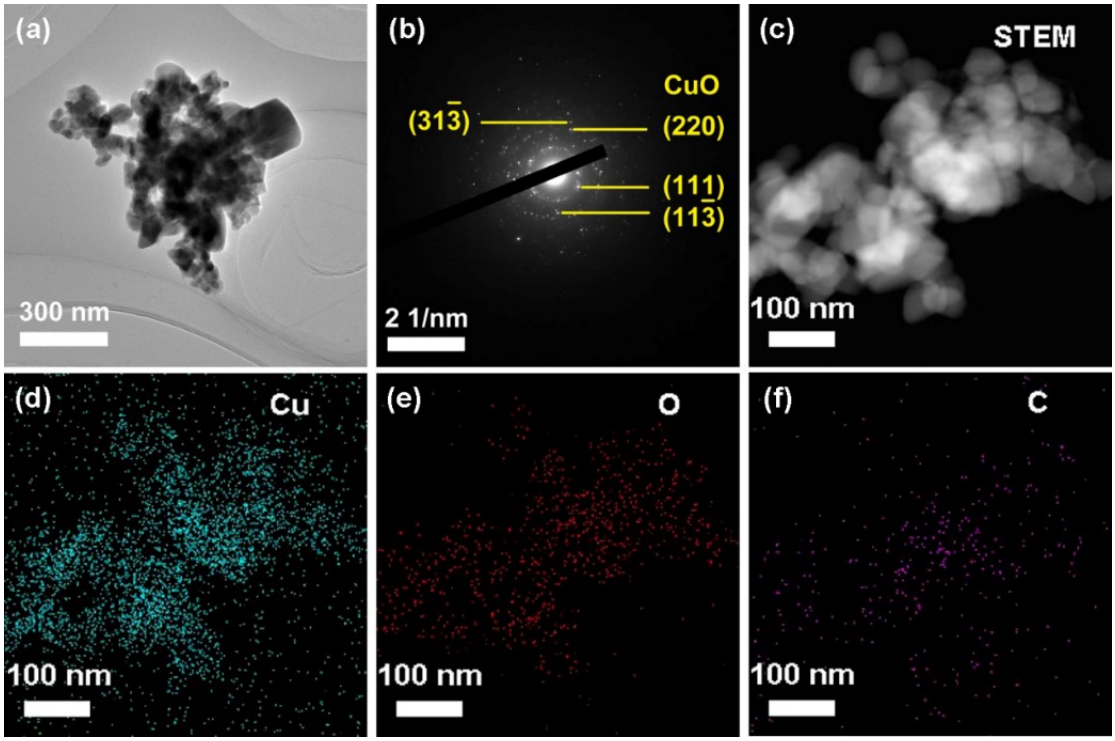

Figure S11. (a) TEM image of Cu400; (b) SAED pattern of Cu400; (c) to (f) HAADF-STEM image and EDS elemental mappings of Cu400.

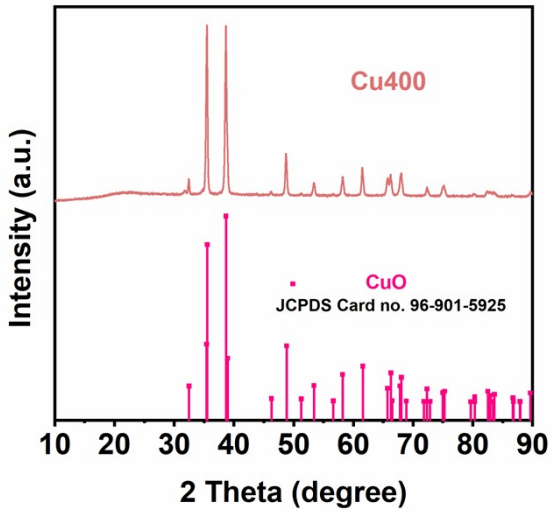

Figure S12. XRD pattern of Cu400.

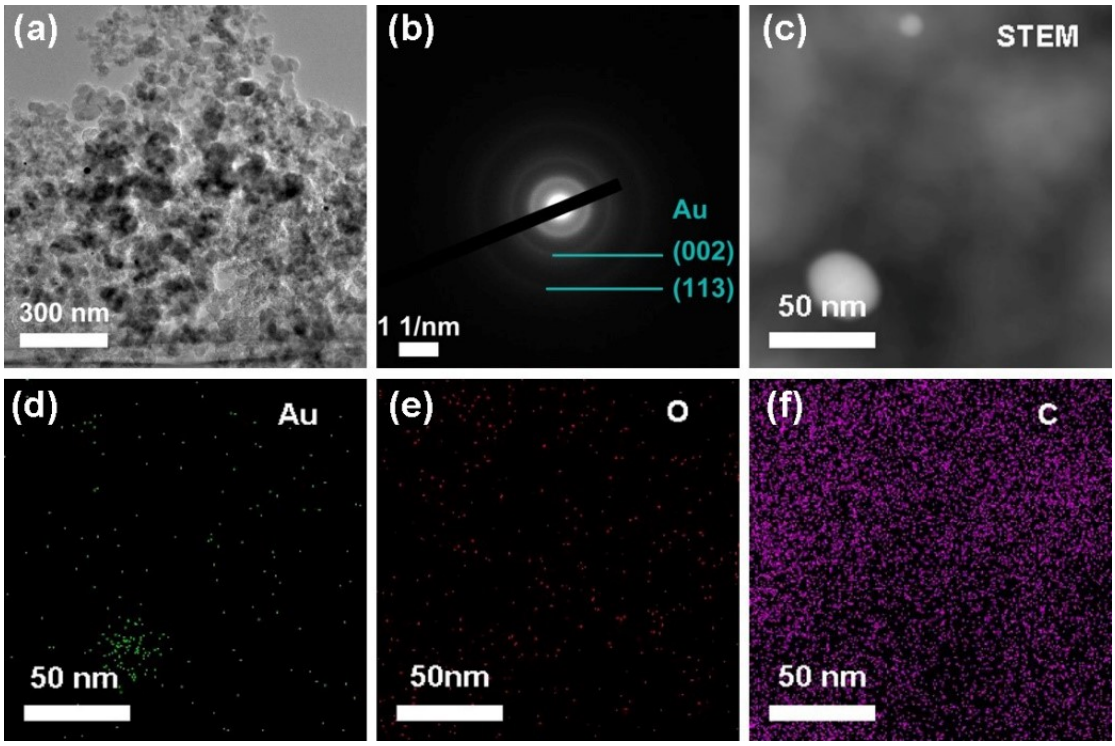

Figure S13. (a) TEM image of Au400; (b) SAED pattern of Au400; (c) to (f) HAADF-STEM image and EDS elemental mappings of Au400.

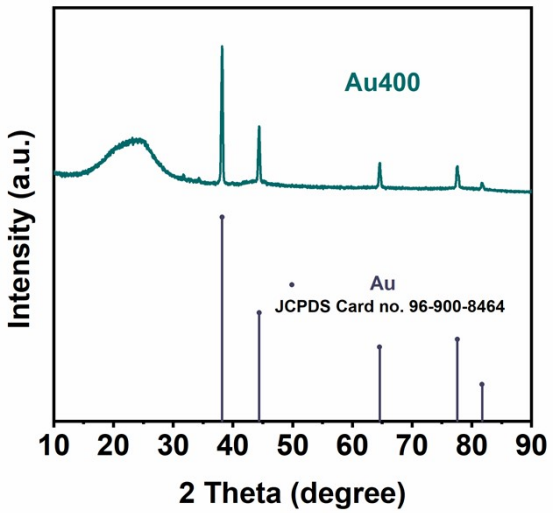

Figure S14. XRD pattern of Au400.

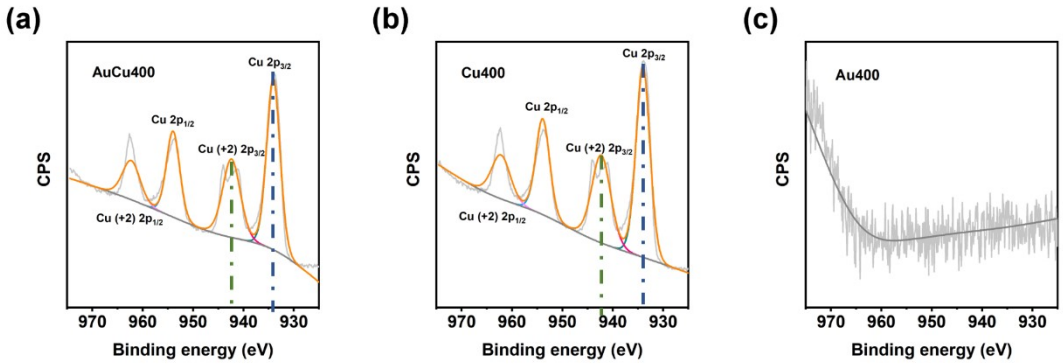

Figure S15. Cu 2p XPS spectra of (a) AuCu400, (b) Cu400 and (c) Au400.

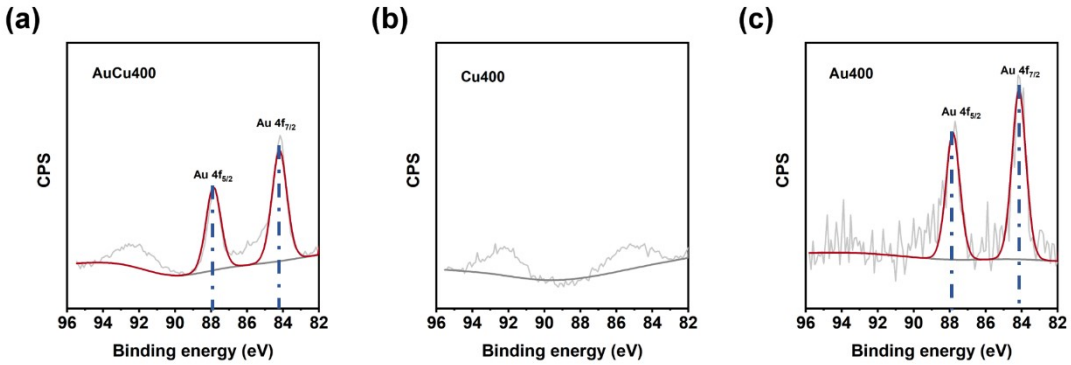

Figure S16. Au 4f XPS spectra of (a) AuCu400, (b) Cu400 and (c) Au400.

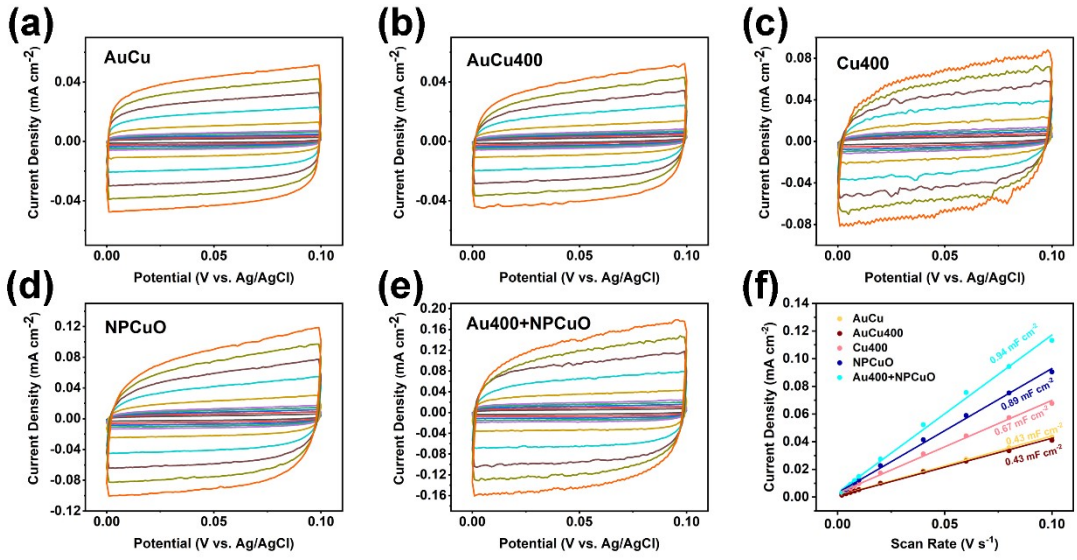

Figure S17. CV curves of (a) AuCu, (b) AuCu400, (c) Cu400, (d) NPCuO and (e) Au400+NPCuO, and (f) plots of current density versus scan rate of them.

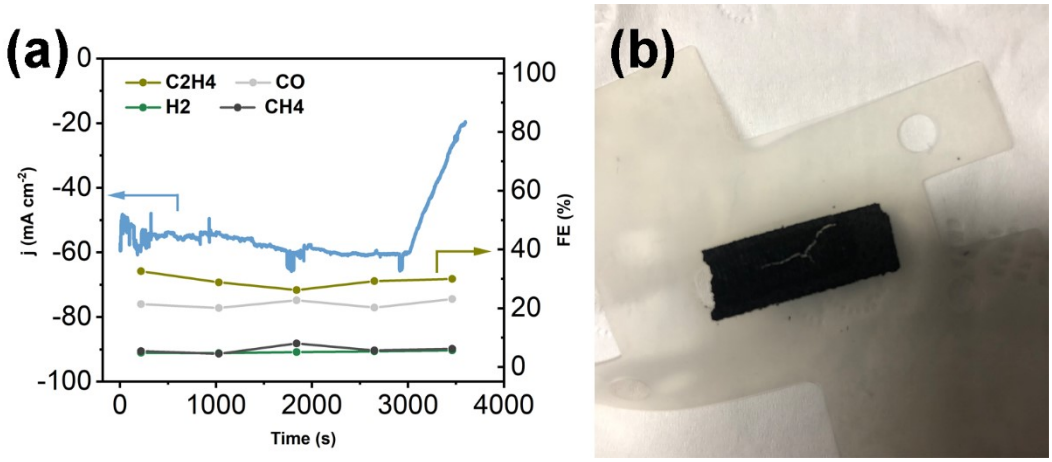

Figure S18. (a) Time-dependent current density curve and FE_{C2H4}, FE_{CO}, FE_{H2} and FE_{CH4} of AuCu400 in 1 M KOH solution at -1.0V; (b) photos of the broken carbon paper-based gas diffusion electrodes after the test.

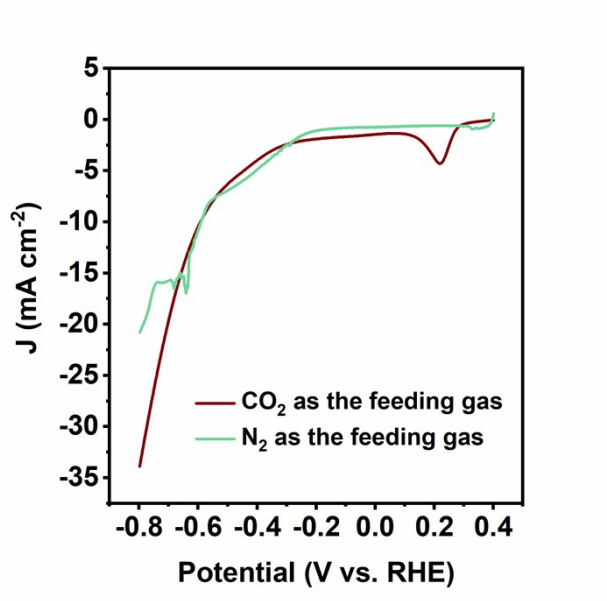

Figure S19. LSV curves of AuCu400 using CO_2 or N_2 as the feeding gas and 1 M KOH aqueous solution as the electrolyte.

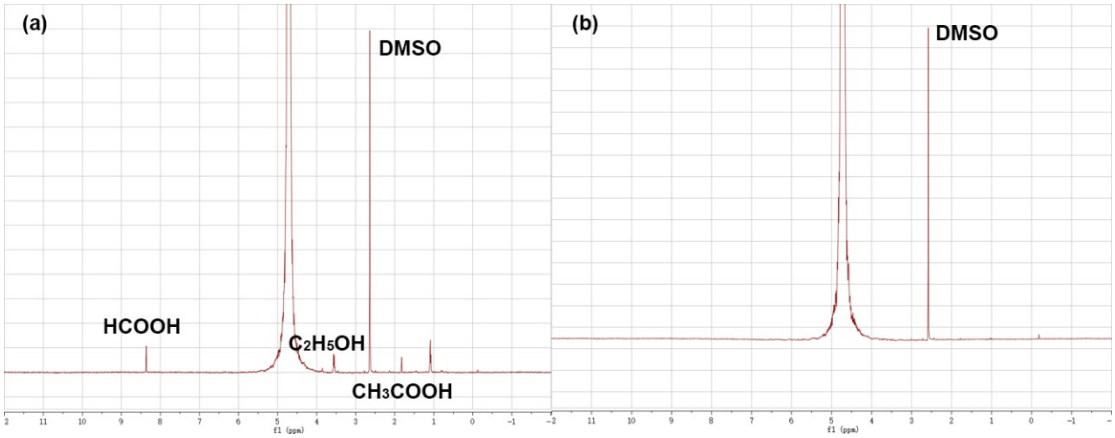

Figure S20. ^{1}H NMR spectra of the electrolyte after electrolysis at -1.0 V vs. RHE for AuCu400 using (a) CO_2 or (b) N_2 as the feeding gas and 1 M KOH aqueous solution as the electrolyte.

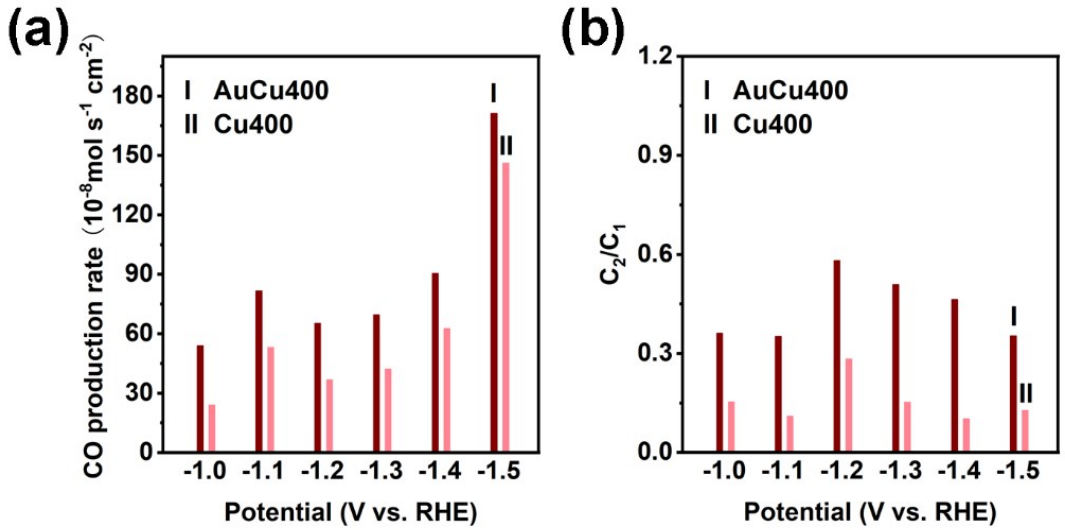

Figure S21. (a) The CO production rates and (b) the ratios of C_{2+} to C_1 products of AuCu400 and Cu400.

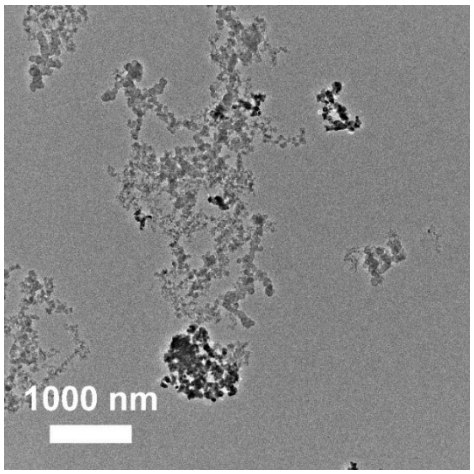

Figure S22. TEM image of Au400+Cu400.

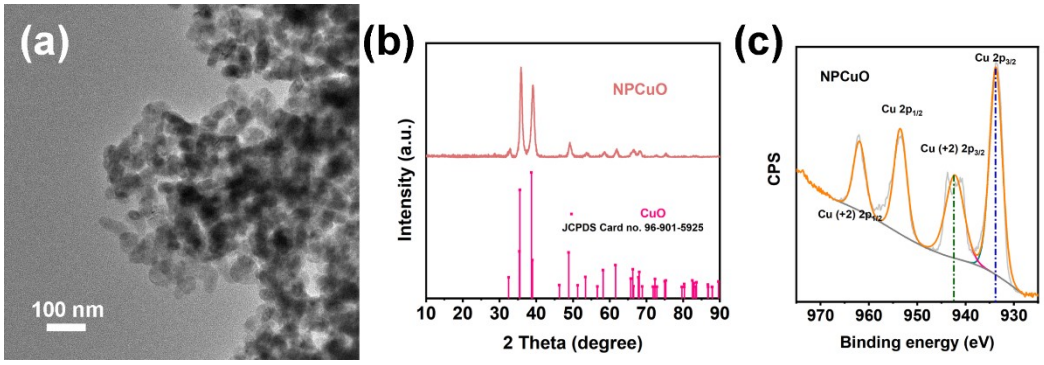

Figure S23. (a) TEM image, (b) XRD pattern and (c) Cu 2p XPS spectra of NPCuO.

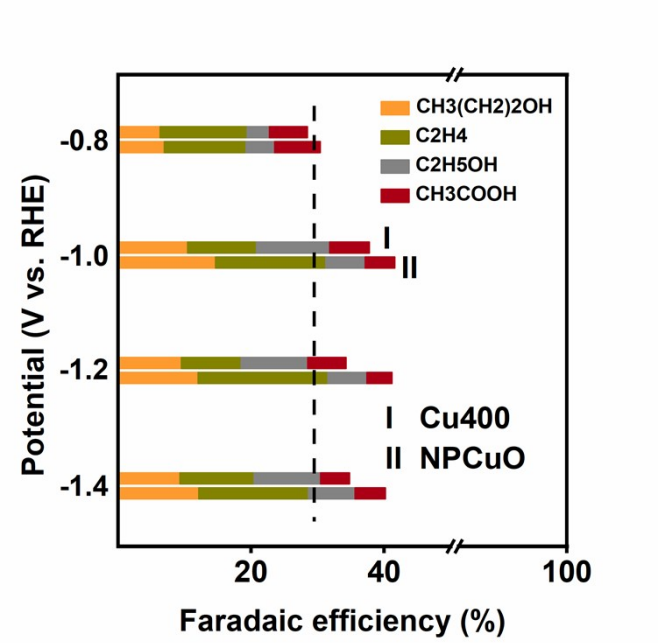

Figure S24. C_{2+} products FEs of Cu400 and NPCuO using CO as the feeding gas.

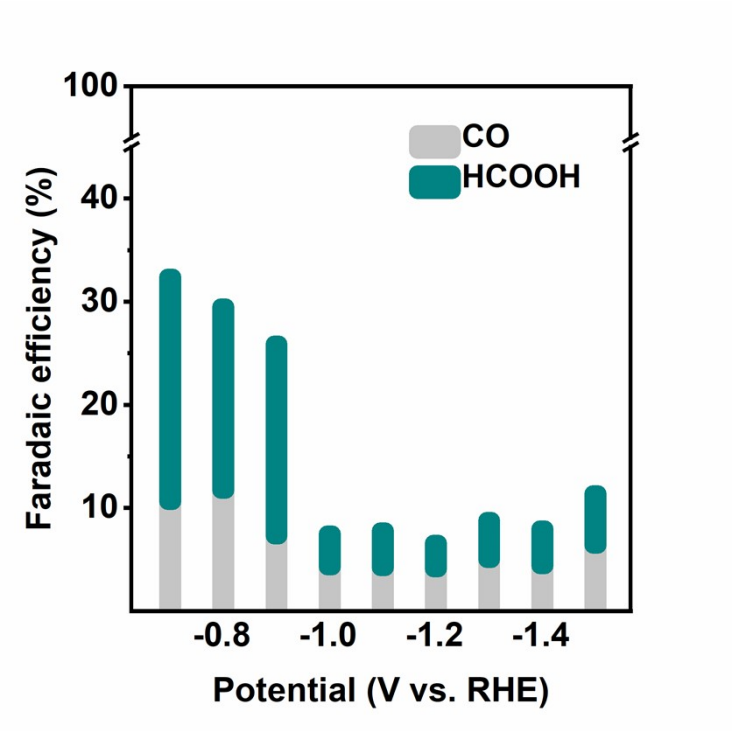

Figure S25. CO_2 reduction products FE of Au400 using CO_2 as the feeding gas.

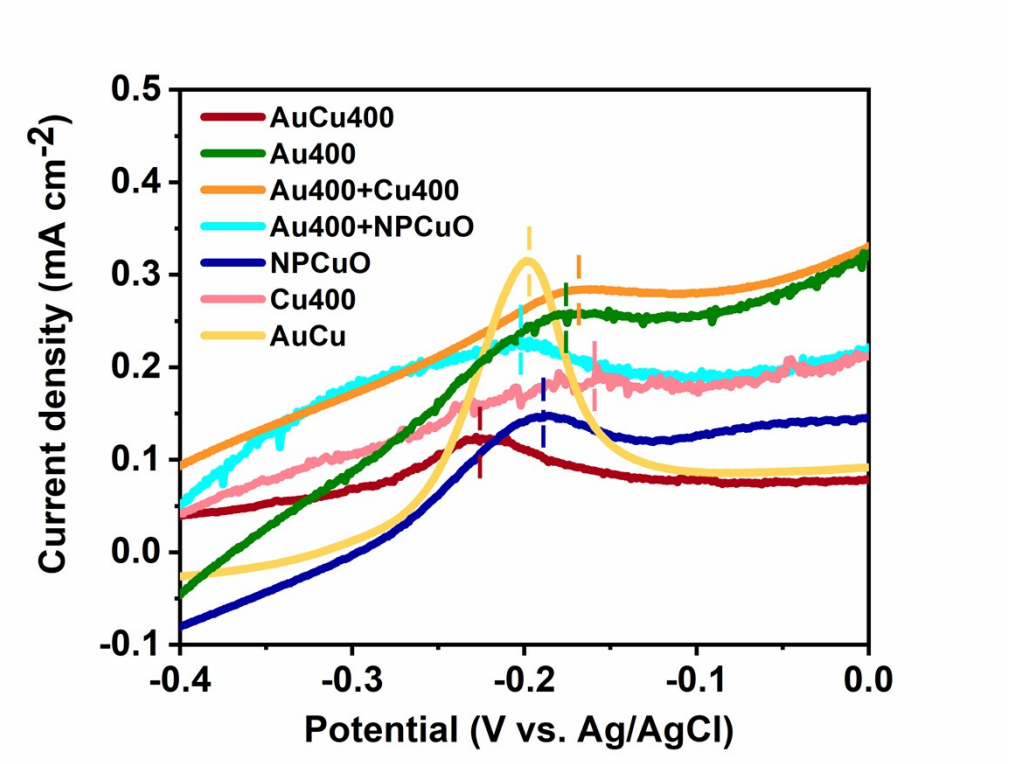

Figure S26. Oxidative LSV scans in N_2-saturated aqueous 1 M KOH solution of AuCu400, Au400, Cu400, AuCu, NPCuO, Au400+Cu400 and Au400+NPCuO.

Supplementary Tables

Table S1. H_2 FE of samples in the articles at applied potentials (V vs. RHE).

	-1.0	-1.1	-1.2	-1.3	-1.4	-1.5
AuCu400	**4.8%**	**12.9%**	**12.0%**	**12.9%**	**16.3%**	**13.1%**
Cu400	21.0%	21.2%	19.6%	27.3%	23.8%	43.1%
Au400	59.8%	58.7%	56.0%	58.6%	59.4%	58.1%
AuCu	19.5%	32.5%	31.9%	24.5%	33.7%	21.5%
Au400+NPCuO	31.4%	21.7%	23.1%	18.8%	24.7%	30.5%
Au400+Cu400	35.7%	48.9%	38.1%	32.1%	41.4%	40.5%
NPCuO	24.1%	25.2%	31.0%	31.1%	34.5%	34.8%

Table S2. C_{2+} Products Faradaic efficiency of Au-Cu-based eCO_2RR electrocatalysts reported in the literatures.

	FE	Potential (V vs. RHE)	Ref
S2-1 Au-Cu tandem			
Au NPs on Cu foil	C_2H_5OH 25.18%	-0.97	29
Au NBP-Cu JNCs	C_2H_4 & C_2H_6 46.4%	-0.98	30
AuCu	C_{2+} 70.1%	-1.05	31
Au@Cu_2O	C_2H_5OH 52.3%	-0.3	S1
Au and Cu lines device	C_{2+} ~56%	-1.0	S2
$Au_{0.02}Cu_2O$	C_2H_4 24.4%	-1.3	S3
Au/CuO-CuO	**C_2 52.8%**	**-1.0**	**This work**
S2-2 Au-Cu for C_1			
AuCu NPs	CO 80%	-0.77	32
Au_3Cu Cu_3Au	CO ~60%	-0.7 ~ -1.1	34
hollow Au-Cu NPs	CO 53.3%	-0.7	35
Au-Cu nanowire	CO & HCOOH ~40%	-1.0 vs. SHE (0.1 M $NaHCO_3$)	S4
Au_3Cu	CO 98.12%	-0.7	S5
Cu/Au	HCOOH 81%	-0.6	S6
S2-3 Au-Cu for C_2 (alloying effect, electronic effect and geometric effect)			
4H/*fcc* Au@Cu	C_2H_4 46.7%	-1.17	S7
AuCu alloy NPs	C_2H_4 & C_2H_5OH 44%	-1.0	S8
$Cu_{63.9}Au_{36.1}$/NCF	C_2H_5OH 12%	/	S9

Supplementary References

S1 B. Zhang, Y. Wang, S. Xu, K. Chen, Y. Yang, Q. Kong, Tuning nanocavities of Au@Cu_2O yolk-shell nanoparticles for highly selective electroreduction of CO_2 to ethanol at low potential, *RSC Advances*, 2020, **10**, 19192-19198.

S2 Y. Lum, J. W. Ager, Sequential catalysis controls selectivity in electrochemical CO_2 reduction on Cu, *Energy & Environmental Science*, 2018, **11**, 2935-2944.

S3 X. Cao, G. Cao, M. Li, X. Zhu, J. Han, Q. Ge, H. Wang, Enhanced ethylene formation from carbon dioxide reduction through sequential catalysis on Au decorated cubic Cu_2O electrocatalyst, *European Journal of Inorganic Chemistry*, 2021, **2021**, 2353-2364.

S4 B. A. Zhang, D. G. Nocera, Cascade electrochemical reduction of carbon dioxide with bimetallic nanowire and foam electrodes, *ChemElectroChem*, 2021, **8**, 1918-1924.

S5 X. Ma, Y. Shen, S. Yao, M. Shu, R. Si, C. An, Self-supported nanoporous Au_3Cu electrode with enriched gold on surface for efficient electrochemical reduction of CO_2, *Chemistry-A European Journal,* 2020, **26**, 4143-4149.

S6 Z. Tao, Z. Wu, X. Yuan, Y. Wu, H. Wang, Copper-gold interactions enhancing formate production from electrochemical CO_2 reduction, *ACS Catalysis*, 2019, **9**, 10894-10898.

S7 Y. Chen, Z. Fan, J. Wang, C. Ling, W. Niu, Z. Huang, G. Liu, B. Chen, Z. Lai, X. Liu, B. Li, Y. Zong, L. Gu, J. Wang, X. Wang, H. Zhang, Ethylene selectivity in electrocatalytic CO_2 reduction on Cu nanomaterials: A crystal phase-dependent study, *J Am Chem Soc*, 2020, **142**, 12760-12766.

S8 S. Shen, X. Peng, L. Song, Y. Qiu, C. Li, L. Zhuo, J. He, J. Ren, X. Liu, J. Luo, AuCu alloy nanoparticle embedded Cu submicrocone arrays for selective conversion of CO_2 to ethanol, *Small*, 2019, **15**, e1902229.

S9 F. Jia, X. Yu, L. Zhang, Enhanced selectivity for the electrochemical reduction of CO_2 to alcohols in aqueous solution with nanostructured Cu-Au alloy as catalyst, *Journal of Power Sources*, 2014, **252**, 85-89.